Task 1.2

Title

Reservoir stimulation and engineering

Projects (presented on the following pages)

Evaporitically-triggered thermo-haline circulation and its influence on geothermal anomalies near unconformities
Julian Mindel

High-resolution temporo-ensembe PIV to resolve pore-scale flow in fractured porous media
Mehrdad Ahkami, Thomas Roesgen, Martin O. Saar, Xiang-Zhao Kong

Fracture process zone in anisotropic rock
Nathan Dutler, Morteza Nejati, Benoît Valley, Florian Amann

On the variability of the seismic response during multiple decameter-scale hydraulic stimulations at the Grimsel Test Site
Linus Villiger, Valentin Gischig, Joseph Doetsch, Hannes Krietsch, Nathan Dutler, Mohammedreza Jalali, Benoit Valley, Florian Amann, Stefan Wiemer

Does a cyclic fracturing process agree with a fluid driven fracture solution?
Nathan Dutler, Benoît Valley, Valentin Gischig, Linus Villiger, Joseph Doetsch, Reza Jalali, Florian Amann

Investigation on Hydraulic Fracturing of Granite
Arabelle de Saussure

Advances in laboratory investigation of fluid-driven fractures
Thomas Blum, Brice Lecampion

Building a geological model for analysis and numerical modelling of hydraulic stimulation experiments
Hannes Krietsch, J. Doetsch, V. Gischig, M.R. Jalali, N. Dutler, F. Amann and S. Loew

SCCER-SoE Annual Conference 2018

Evaporitically-triggered thermo-haline circulation and its influence on geothermal anomalies near unconformities

Julian Mindel, Institute of Geochemistry and Petrology, ETH Zurich

Supported by: Schweizerische Eidgenossenschaft, Confédération suisse, Confederazione Svizzera, Confederaziun svizra. Swiss Confederation. Innosuisse – Swiss Innovation Agency

Abstract / Background

We hypothesize that downward flow of cooler basin brines may displace and mobilize stagnant, hotter, chemically stratified, and often fracture-hosted brines in sediment-covered basements. Previous conceptual studies postulated fingering as a major hydraulic mechanism allowing for mutually up-/and downward flows of brines from the two reservoirs. We assume this is a potential key factor in establishing geothermal anomalies as well as the formation of basin-hosted ore deposits.
We have thus created the prototype of a hydrothermal simulation tool in which faults and fractures can be explicitly represented within a porous matrix. To understand how geometric complexity of the fractures affects thermo-haline transport, we performed a series of simulations utilizing an accurate equation of state. We designed synthetic geometries to study the propagation of salinity fronts using a simulator based on the CSMP++ library (Paluszny et al., 2007), honoring the governing equations for compressible porous media flow and saline transport (Geiger et al., 2006; Weis et al., 2014).
This work is a further step towards modeling thermo-haline convection within realistic representations of discrete networks of thin fractures, a scenario typically observed in basement rocks of deep geothermal systems and at basement/sediment interfaces and related deposits of U, Pn, Zn, and others.

Conceptual Model

The sequence of events remains debatable in some aspects and could be site-specific. In general, we assume that the heavier and oxidizing/acidic new brine originating from the evaporating sea invades the more permeable basin rock and establishes flow.

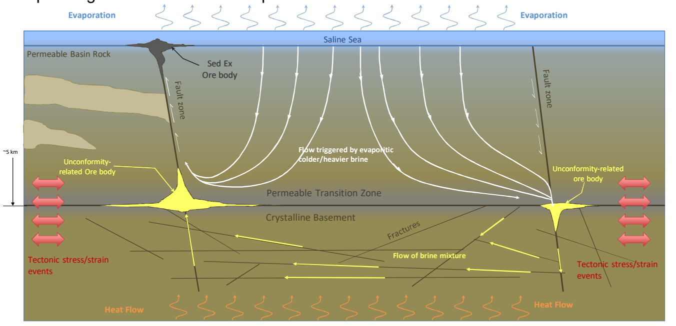

Figure 1 :*Conceptual model showing at least two main available flow mixing paths created by invading evaporitic brines.*

Neglecting any transient effects of tectonics, at least two types of flow paths may form:

1. Invading evaporitic brines mix with and push mineral-rich basin brines upwards via a highly permeable conduit in an "excavating" fashion. Thus, different minerals should form along the flow path at different depths and into what is known as sedimentary exhalative type of deposits.
2. The invading brine, mixed with metal-rich basinal brines, flows into the fractured basement. The new, basinal, and basement brines mix and push out reducing/alkaline basement brines through available exits of the existing basement fracture network.

The permeable transition zone, due to its relatively higher permeability and porosity, acts as a chemical interface for the mixing of brines (i.e. new, basinal, basement) thus contributing to localized redox reactions. Due to temperature, pressure, medium (in terms of pore-space, permeability, and chemistry), and mixing flow conditions, thermal anomalies also very likely to form on and around intersections of fractures and the permeable transition zone.

Governing Equations, Boundary & Initial Conditions

We assume compressible single phase flow in porous media, and thus the continuum governing equations may be written as follows,

$$\mathbf{v} = -\frac{k}{\mu}(\nabla p - \rho_f \mathbf{g}) \quad \longleftarrow \text{ Darcy}$$

$$\frac{\partial(\rho_f \phi)}{\partial t} + \nabla \cdot (\rho_f \mathbf{v}), + q_{\rho_f} = 0 \quad \longleftarrow \text{ Mass}$$

$$\frac{\partial(\phi \rho_f h_f)}{\partial t} + \nabla \cdot (\rho_f h_f \mathbf{v}) = 0$$

$$C_{p,t}\frac{\partial T}{\partial t} - \nabla \cdot (\lambda_t \nabla T) + q_H = 0 \quad \text{Energy}$$

$$\frac{\partial(\phi \rho_f X)}{\partial t} + \nabla \cdot (\rho_f X \mathbf{v}), + q_{\rho_f X} = 0 \quad \longleftarrow \text{ Salinity}$$

Density, enthalpy, and heat capacity are all functions of pressure, temperature, and mass fraction of NaCl. While neglecting salinity diffusion, we also consider the material properties of the porous rock to be isotropic, uniform, and constant. The initial pressure, temperature, and salinity profiles are considered stable, and the mesh we use is static.
We designed synthetic models with a low permeability matrix in the basement, many permeable fractures, and several faults zones. Each one of these regions is assigned independent material properties, including a "thickness" value, to allow dimensional consistency with LDE's.
In all our models, we set up time-invariant Dirichlet conditions for pressure and temperature in the top boundary, and a heat flux boundary condition at the bottom boundary. In contrast, the boundary condition for NaCl mass fraction is initially stable at 5% for the first 10000 years (i.e. simulated time), followed by a time varying period 10000 years. This time-varying period begins at 5% and grows to 25% during the first 1000 years, remains steady for the next 8000, and tapers off back to 5% for the next 1000. The aim is to simulate a period of high evaporation followed by sea replenishment.

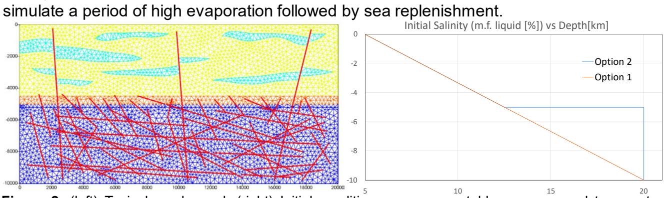

Figure 2: (left) Typical mesh used. (right) Initial conditions assume a stable pressure and temperature profile, while the initial salinity profile varies from 5% at the top to 20% at the bottom.

Results

We set up two separate fluid-tracking tracers: one for the evaporitic brine and the other aimed at the basement brine. With the help of the tracers, as well as temperature conditions, we set up two markers (shown in teal for Marker 1 and orange for Marker 2 in Figures 3 and 4) so that we may approximate and observe the level of mixing.

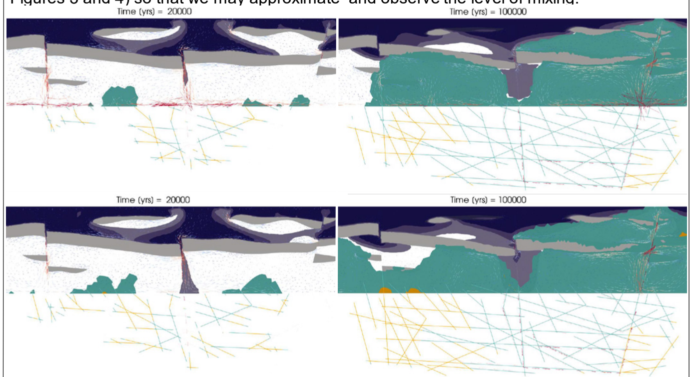

Figure 3:*Result snapshots at the end of the evaporation stage (left) and end of simulation (right) with (top row) and without (bottom row) a permeable transition zone. A dark blue tracer is set to track incoming fluid from the top boundary. Through-going basin Obstacle permeability is 10^-17*

Marker 1 tracks locations in the domain where both the new and basement brine content are above 3% (that is, the total fluid mass fraction of the liquid is 6% basement + new brine, the rest (most of it) is basinal brine) and the temperature is at least 50ºC. Marker 2 follows a similar philosophy, restricting the conditions to 10% (5% of new brine and 5% of basement brine) and the temperature to a typical (at least in the Uranium case) ore forming 130ºC. It also restricts its tracking to the permeable transition zone, which is where it is assumed that the likelihood of precipitation is the highest.

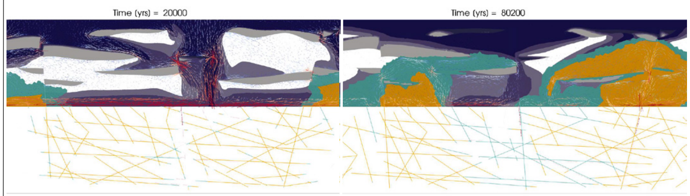

Figure 4: *Result snapshots at the end of the evaporation stage (left) and end of simulation (right) with a permeable transition zone. Obstacles in sedimentary basin either spread-out in this case. Obstacle permeability is 10^-17*

The low percentages used in the markers arise from the fact that the only portion of basement brine that is truly mobile is in the fractures, which corresponds to a relatively small amount of the total brine content in the domain, and that the "new" incoming brine is only being fluxed in for a limited time. Most of the mobilized fluid consists of pre-existing basinal brine, which is the richest and metal-bearing one. While the markers do not track actual precipitation because we have not used reactive transport modelling features for this study (i.e. yet!), they indicate where it is very likely that precipitation may happen.
Figure 5 shows a snapshots of a simulation that differs from Figure 3 (top row) only in its initial salinity profile (i.e. using "option 2" from Figure 2). Such a scenario assumes that basement brine salinity is much higher than that of a linear-with-depth profile.

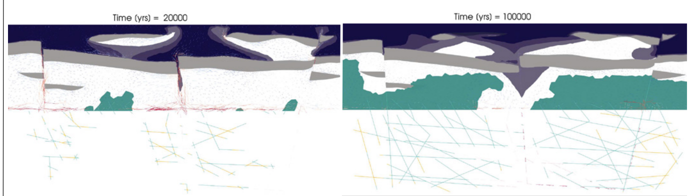

Figure 5:*Result snapshots at the end of the evaporation stage (left) and end of simulation (right) with a permeable transition zone and through-going obstacles. Simulation is identical to Figure 3 (top row) with a constant initial salinity m.f. of 0.2 in the basement (see Figure 2 - Initial salinity profile, Option 2).*

Conclusions & Outlook

Temperature, pressure, and salinity, together with medium pore-space and permeability create the mixing flow conditions which, as expected, show a particular predilection for the vicinity of unconformities.
We established slightly more-complex-than proof of concept simulations in a bid to understand the onset of geothermal anomalies in particular circumstances/scenarios. Results show promise by pointing out probable locations with the help of markers, which help track pre-selected conditions. They also serve to highlight the importance of initial conditions, sedimentary "obstacle" permeability, and the numerous possible scenarios that would need to be simulated, carrying out a sensitivity analysis, all of which is still needed prior to drafting any strong conclusions.

References

1. Geiger, S. et al.(2006) Transport in Porous Media, 63, 399–434, doi: 10.1007/s11242-005-0108-z
2. Paluszny, A. et al (2007) Geofluids, 7: 186–208.
3. Weis, P. et al. (2014), Geofluids, 14(3): 347–371,doi: 10.1111/gfl.12080

SCCER SoE
SWISS COMPETENCE CENTER for ENERGY RESEARCH
SUPPLY of ELECTRICITY

SCCER-SoE Annual Conference 2018

Supported by:
Schweizerische Eidgenossenschaft
Confédération suisse
Confederazione Svizzera
Confederaziun svizra
Swiss Confederation
Innosuisse – Swiss Innovation Agency

High-resolution temporo-ensembe PIV to resolve pore-scale flow in fractured porous media

Mehrdad Ahkami, Thomas Roesgen, Martin O. Saar, Xiang-Zhao Kong

Motivation Fractures are conduits that can enable fast advective transfer of (fluid, solute, reactant, particle, etc.) mass and energy. Such fast transfer can significantly affect pore-scale physico-chemical processes which in turn can affect macroscopic mass and energy transport characteristics. Therefore, it is crucial to determine pore-scale transport properties and then upscale these properties to larger scales. However, only a limited number of experimental studies with sufficient spatial resolution over large Representative Elementary Volumes have been conducted to characterize fluid flow and transport features in fractured porous media.

Methodology

Experimental setup: In this study, 3D-printing technology is employed to manufacture a transparent fractured porous medium to resemble dual-permeability and dual-porosity subsurface formations. Square pillars with a size of 800 µm are 3D-printed to construct fractured porous matrices inside the cell. Parallel to the main flow direction, the cell is divided into two halves: one half being a high-permeability matrix with 300 µm spacing between the pillars and the other half being a low-permeability matrix with 200 µm spacing between the pillars. Moreover, we embed one flow-through fracture and one dead-end fracture within each porous matrix. The permeabilities of two matrices are ~4.0 × 10^{-9} m^2 and ~7.5 × 10^{-9} m^2, respectively.
Due to an in-line illumination configuration, the seeding particles in the fluid cast shadows on a bright background. We then use Particle Shadow Velocimetry (PSV) method to optically resolve the fluid flow.

Temporo-ensemble PIV: Classical PIV method generally employs a relatively large interrogation window and can thus not resolve pore-scale micro-features of fluid flow. In this study, we introduce a new high-resolution PIV method that we term "temporo-ensemble PIV" that can reduce the size of the interrogation window down to ultimately one single pixel. Such a small interrogation window size enables substantially increased spatial resolutions of velocity vectors per unit area in 2D (or unit volume in 3D), allowing delineations of small, pore-scale flow features that are part of a much larger Field of View (FOV). We apply our new method to visualize a 2D fluid flow in a 3D-printed, fractured porous medium.

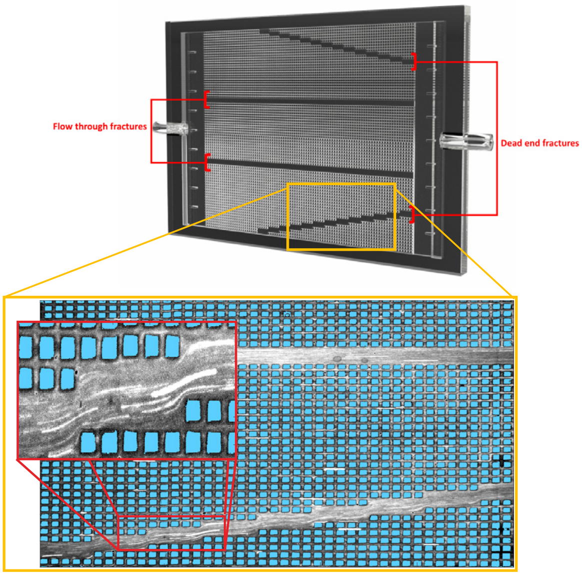

A time-lapse image of particle trajectories, captured during a time interval of 25 sec. The whiteness quantifies the particle density. Blue patches indicate the masks which are applied to exclude regions of impermeable pillars during the PIV calculations.

Results

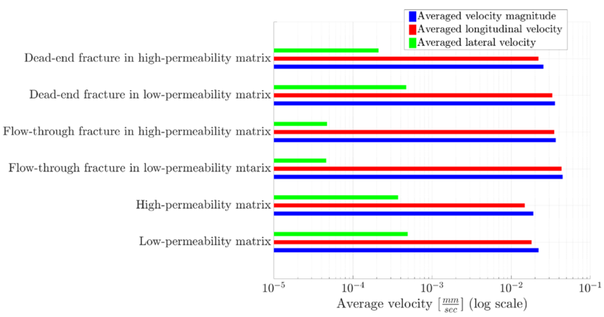

Average Velocity magnitude, average longitudinal velocities, and average lateral velocities of low- and high-permeability matrices as well as embedded dead-end and flow-through fractures.

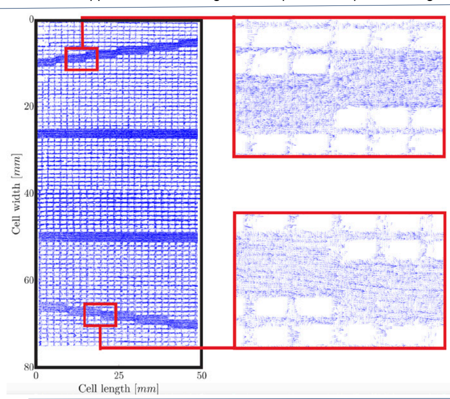

Velocity field of the full field of view, obtained by the temporo-ensemble method. Enlargement of velocity field in the dead-end fracture embedded in the low-permeability matrix (top-right) and the dead-end fracture embedded in the high-permeability matrix (bottom-right).

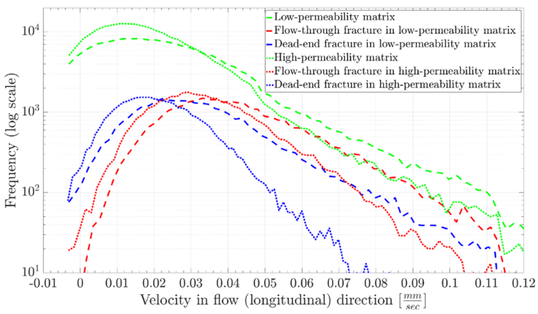

Histogram of longitudinal velocities in different regions of the afore-mentioned fractured porous media

Conclusion

- The presented approach can resolve high-resolution 2D velocities in engineered porous media with various levels of heterogeneities.
- Compared to standard PIV methods, our approach preserves high spatial resolutions of velocity vectors, while enabling a large field of view.
- The resulting high-resolution velocity vectors delineate detailed 2D fluid flow structures in various regions of the 3D-printed fractured porous medium. This enables the analysis of various flow interactions, such as those between porous matrices, with different permeabilities and/or porosities, or between fractures and their surrounding porous matrices.
- Our work facilitates experimental investigations of pore-scale physico-chemical processes, with implications for various industrial and scientific fields such as the oil and gas industry, hydrogeology, geothermics, geochemistry.

SCCER-SoE Annual Conference 2018

SCCER SoE
SWISS COMPETENCE CENTER for ENERGY RESEARCH
SUPPLY of ELECTRICITY

UNIVERSITÉ DE NEUCHÂTEL

ETH zürich

RWTH AACHEN UNIVERSITY

Supported by:
Schweizerische Eidgenossenschaft
Confédération suisse
Confederazione Svizzera
Confederaziun svizra

Swiss Confederation

Innosuisse – Swiss Innovation Agency

Fracture process zone in anisotropic rock

Nathan Dutler, Morteza Nejati**, Benoît Valley*, Forian Amann****
*Centre for Hydrogeology and Geothermics, University of Neuchâtel
** Department of Earth Sciences, ETH Zurich
*** Chair of Engineering Geology and Environmental Management, RWTH Aachen, Germany

1. Motivation

This experimental work aims at assessing the dependency of the **fracture process zone (FPZ)** on the angle between the fracture growth direction and the anisotropy (foliation) for the Grimsel Granodiorite. Samples were collected from cores of the In-situ Stimulation and Circulation project (Amann et al., 2018) and tested using a notched semi-circular bending (NSCB) method. The foliation consist essentially of aligned phylosilicate minerals.

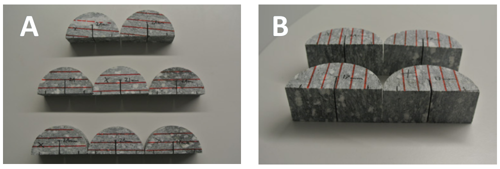

Figure 1: A) and B) presents the two endmembers with the foliation aligned (φ=90°) and normal (φ=0°) to the artificial notch.

2. Methods

Three-point-bending tests on notched semi-circular specimens (Kuruppu et al., 2014) were performed. The deformation field of the specimens was monitored using Digital Image Correlation (DIC).

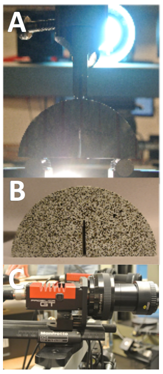

- **15 specimens** are tested with 2 different configurations (0°, 90°)
- A **quasi-static load** was applied with controlled displacement rate of 0.1 mm/min
- Specimens are colored in white and afterwards fine sparkled with an air brush (Figure 2B)
- Stereo Digital Image Correlation (DIC) is used to get the strain field with a frequency of 4 Hz during the tests (Cam 1 + 2)

Figure 2: A) Zwick universal testing machine with view on the sample side. B) sparkled specimen for DIC C) The DIC system with two Prosilica GT3400 (red)

3. Localized FPZ at peak load

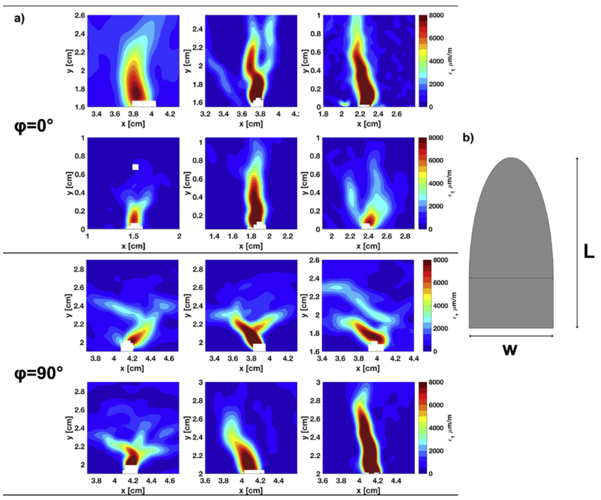

Figure 3: (a) The contours of maximum principal strain showing the FPZ shape at peak load for the configurations $\varphi = 0°, 90°$. (b) The FPZ at the peak load is idealized schematically as a semi-elliptical region with the width of W and the length of L (Dutler et al., 2018).

4. Width of the FPZ and critical strain

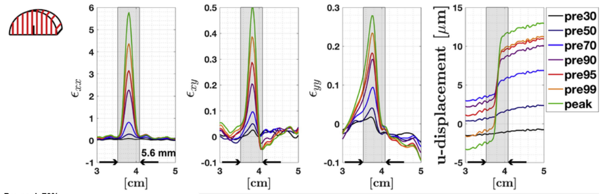

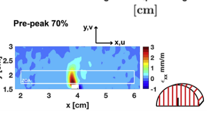

Figure 4: The calculation of the FPZ width based on localization of strain components ϵ_{xx},ϵ_{xy},ϵ_{yy}, given in millistrain (mm/m) and the jump of displacement u for $\varphi = 0°$ at seven different loading stages prior to the peak load. The width of the FPZ corresponds to the width of the shaded region and measures w = 5.6 mm for φ=0°. The width of the FPZ is picked using a zone of averaging (ZOA) at 70% of pre-peak load. According to the coordinate system shown, negative values of displacement imply movements to the left (Dutler et al., 2018).

It is noteworthy that according to the values of tensile strength and Young's moduli, a **critical tensile strain** of about 270 and 350 micro strains are obtained for the principal directions normal and parallel to the foliation.

$$\sigma_t = E\epsilon_c$$

φ	σ_t	E	ϵ_c
0°	5.63	21	270
90°	14.69	42	350

From the ϵ_{xx} plot in Fig. 4, it is seen that such values of critical strain are exceeded **at a loading stage between 50% and 70% of the peak load**. This loading level is in a very good agreement with the general belief that the development of inelastic deformation of quasi-brittle materials start at about 60–70% of the peak load.

5. The size of the FPZ

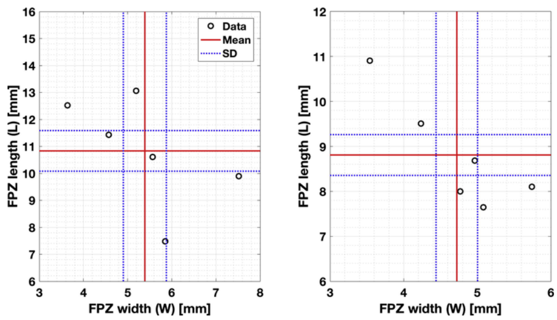

Figure 5: The measured values for the FPZ width (W) and length (L) for two cases of $\varphi = 0°$ and $\varphi = 90°$. The mean values of the six tests are shown by red line, while the blue pointed line show the standard deviation. The results are taken from the fully formed FPZ, i.e. at 70% of pre-peak load for $\varphi = 0°$ and 90% of pre-peak load for $\varphi = 90°$ (Dutler et al., 2018).

- In both configurations $\varphi = 0°$ and $\varphi = 90°$, the average length to width ratio is L/W≈2.
- The fracture process zone is larger in size when the crack grows along the foliation compared to the case it propagates normal to the foliation. The ratio of the FPZ size in two directions is $L_{\varphi = 0°}/L_{\varphi = 90°} \approx W_{\varphi = 0°}/W_{\varphi = 90°} \approx 1.2$. The fracture process zone is anisotropic in terms of size.
- The reason for a bigger FPZ along the foliation may be the preferred direction of micro-crack in such direction. Since the micro-cracks are oriented in the direction of crack growth, their activation and propagation can lead to a wider process zone.
- There is a negative correlation between the length and the width of the FPZ in both configurations. One can explain this trend by considering that the energy dissipated via micro-cracking is a material property, which is constant.

References

F. Amann, V. Gischig, K. Evans, J. Doetsch, R. Jalali, B. Valley, et al., The seismo-hydromechanical behavior during deep geothermal reservoir stimulations: open questions tackled in a decameter-scale in situ stimulation experiment, Solid Earth 9 (1) (2018) 115–137.

N. Dutler, M. Nejati, F. Amann, B. Valley, and G. Molinari (2018), On the link between fracture toughness, strength and fracture process zone in anisotropic rocks, EFM, (in press). https://doi.org/10.1016/j.engfracmech.2018.08.017

M.D. Kuruppu, Y. Obara, M.R. Ayatollahi, K.P. Chong, T. Funatsu, ISRM-suggested method for determining the mode I static fracture toughness using semi-circular bend specimen, Rock Mech Rock Eng 47 (1) (2014) 267–274.

SCCER SoE
SWISS COMPETENCE CENTER for ENERGY RESEARCH
SUPPLY of ELECTRICITY

SCCER-SoE Annual Conference 2018

ETH zürich

70 NRP Energy Turnaround National Research Programme

Supported by:
Schweizerische Eidgenossenschaft
Confédération suisse
Confederazione Svizzera
Confederaziun svizra
Swiss Confederation
Innosuisse – Swiss Innovation Agency

On the variability of the seismic response during multiple decameter-scale hydraulic stimulations at the Grimsel Test Site

Linus Villiger*, Valentin Gischig**, Joseph Doetsch**, Hannes Krietsch**, Mohammadreza Jalali**, Nathan Dutler ***, Benoît Valley ***, Florian Amann**, Arnaud Mignan* & Stefan Wiemer*

Motivation

Predicting induced seismic activity or even occurring maximum magnitude events for hydraulic stimulation operations, e.g. used to increase transmissivity in reservoirs for deep geothermal systems (EGS), is an extremely challenging task. However, estimating at least induced large magnitude events is indispensable when it comes to the hazard assessment of possible new EGS sites. The main reason for the difficulty of the task is the limited knowledge of geological conditions as well as the in-situ stress state at depth. When it comes to hydraulic stimulation, one distinguishes between hydraulic fracturing (HF), where an induced fracture is propagated through the rock and hydraulic shearing (HS), where slip is induced on pre-existing fractures or faults. During stimulation, the two end-member mechanisms HF and HS occur in a complex interplay (see also talk by H.Krietsch on Friday, 11:45). The driving force, however, for HS on pre-existing structures are tectonic stresses, which hold a high potential for inducing large magnitude seismic events, if the fracture or fault is well oriented to the stress field.

In order to find strategies to mitigate large magnitude events and to better understand the seismo-hydro-mechanical coupled phenomena involved in hydraulic stimulation we performed six HS and five HF experiments in-situ at a decameter scale. In this contribution we focus on the six HS experiments. All experiments were performed in the framework of the In-situ Stimulation and Circulation (ISC) experiment at the Grimsel Test Site (GTS) (Amann et al., 2018).

Methods

The 6 hydraulic stimulation experiments were performed in a 20 x 20 x 20 m crystalline rock volume, in which the stress state and geology was exceptionally well characterized (Figure 1). The experiments targeted ductile shear zones (referred to as S1) as well as brittle-ductile shear zones (S3). These S3 shear zones contain a highly fractured zone in the East. A standardized injection protocol was used for the six HS experiments. In total 1'000 litres of water was injected in every HS experiment. Aside of the high-resolution deformation- and pressure-monitoring networks, a highly sensitive acoustic emission monitoring network was installed (Figure 2).

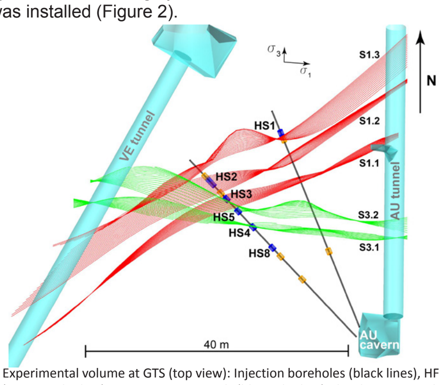

Figure 1: Experimental volume at GTS (top view): Injection boreholes (black lines), HF injection intervals (orange cylinders), HS injection intervals (blue cylinders), the shear zones along with the far field stress state (σ1: ~ 13.8 MPa, plunging to the East with 30 – 40°, σ3: ~ 8 MPa, sub-horizontal North-South, σ₂ = ~ 8.5 MPa, Krietsch et. al, 2018)

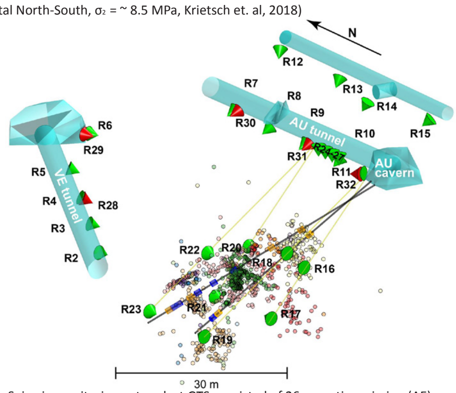

Figure 2: Seismic monitoring network at GTS consisted of 26 acoustic emission (AE) receiver (green cones) and 5 accelerometer (red cones) for calibration purposes along with all located events of the 11 experiments

Results

Table 1 shows an overview of the cumulative number of located events (orange bars) and transmissivity changes (blue bars) of the six HS experiments. The experiments are sorted according to the stimulated structure. Based on the far-field stress state, structures with S1 direction exhibit a larger slip tendency, compared to structures with S3 direction. Note also, that final transimissivities are in the same order of magnitude and generally controlled by S3 structures.

Table 1: Overview located events vs. transmissivity change

Slip tendency

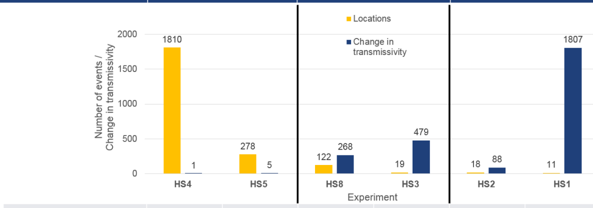

Structure	Shear zone S3		Shear zone S3 and S1		Shear zone S1	
Initial transmissivity [m2/s]:	1.2e-7	1.2e-8	2.8e-10	4.8e-10	2.5e-9	8.3e-11
Final transmissivity [m2/s]:	1.2e-7	5.5e-8	7.5e-8	2.3e-7	2.2e-7	1.5e-7

In Figure 3, frequency magnitude distributions (FMD's) along with b- and a_{fb}-values (activation feedback parameter, Mignan et al., 2017) of all HS experiments are shown. The amplitude magnitudes M_A presented are estimated from amplitudes recorded with the uncalibrated AE receiver (Figure 2) and adjusted to absolute magnitudes M_W estimated from AE receiver/accelerometer pairs installed on a tunnel level. M_C for all experiments was estimated at M_A - 2.8.

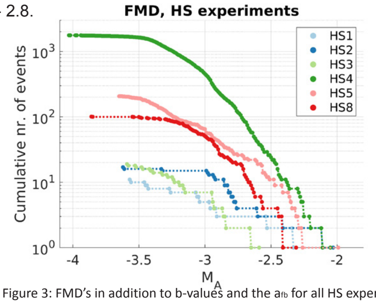

Exp.	b	a_{fb}
HS1	1.13	-2.61
HS2	1.51	-2.96
HS3	2.55	-6.8
HS4	2.5	-4.93
HS5	1.5	-2.72
HS8	2.11	-4.37

Figure 3: FMD's in addition to b-values and the a_{fb} for all HS experiments.

Discussion

A highly variable seismic response (number of seismic events, a_{fb}- and b-values) is observed from six 1'000 l water injections into a small 8'000 m³ crystalline rock volume with variable geology following a standardized injection protocol. Furthermore, there is a tendency that an increased seismic response does not necessarily lead to a higher transmissivity increase. But, out of a far-field stress perspective: a higher slip tendency leads to a higher transmissivity increase.

Furthermore, we can observe that the maximum induced magnitude during the stimulation experiments at Grimsel (Figure 4) does not exceed McGarr's (2014) formulation of the upper bound of the seismic moment of an induced seismic event which is proportional to the total volume of injected fluid.

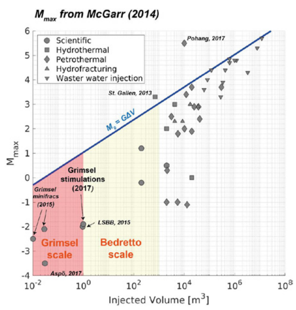

Figure 4: Maximum observed magnitude of induced seismic events of different case studies along with McGarr's (2014) formulation of an upper bound of induced seismic moment.

These outcomes lead to the following questions we would like to tackle in future work:

- What is causing these high variabilities? Is the geology (e.g., increased crack density) the driver for an increased seismic response?
- What can we learn from this scale? Are these findings relevant to the field scale?
- What does this high variability tell us for the predictability of induced seismicity?

References

Amann, F., Gischig, V., Evans, K. F., Doetsch, J., Jalali, R., Valley, B., . . . Giardini, D. (2018). The seismo-hydro-mechanical behaviour during deep geothermal reservoir stimulations: open questions tackled in a decameter-scale in-situ stimulation experiment *Solid Earth*.

Krietsch, H. et al. Stress measurements for an in-situ stimulation experiment in crystalline rock: Integration of induced seismicity, stress relief and hydraulic methods (in review). Rock Mech. Rock Eng. Special Issue: Hydraulic Fracturing of Hard Rock, (2018).

McGarr, A. (2014). Maximum magnitude earthquakes induced by fluid injection. *Journal of Geophysical Research: Solid Earth, 119*(2), 1008-1019.

Mignan, A., Broccardo, M., Wiemer, S., & Giardini, D. (2017). Induced seismicity closed-form traffic light system for actuarial decision-making during deep fluid injections. *Sci Rep, 7*(1), 13607. doi:10.1038/s41598-017-13585-9

SCCER SoE
SWISS COMPETENCE CENTER for ENERGY RESEARCH
SUPPLY of ELECTRICITY

unine UNIVERSITÉ DE NEUCHÂTEL

RWTH AACHEN UNIVERSITY

SCCER-SoE Annual Conference 2018

Supported by:
Schweizerische Eidgenossenschaft
Confédération suisse
Confederazione Svizzera
Confederaziun svizra
Swiss Confederation
Innosuisse – Swiss Innovation Agency

ETH zürich

Does a cyclic fracturing process agree with a fluid driven fracture solution?

Nathan Dutler*, Benoît Valley, Valentin Gischig, Linus Villiger, Hannes Krietsch, Joseph Doetsch, Reza Jalali & Florian Amann

1. Motivation

Observation of two stick-split like behaviour in the **pressure response interval PRP13** during the hydraulic fracturing experiment as part of the In-situ Stimulation and Circulation (ISC) project executed in the Grimsel Test Site.

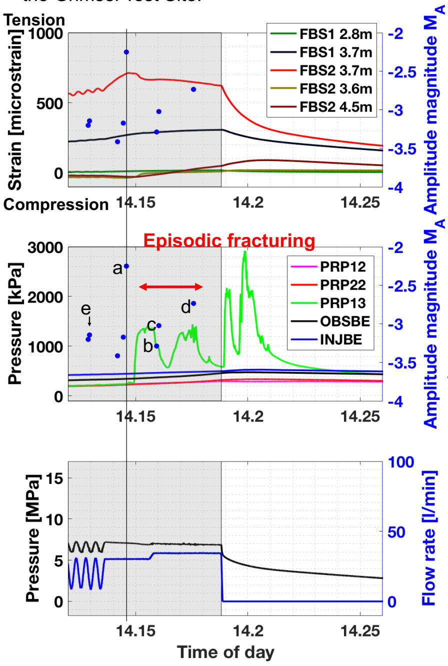

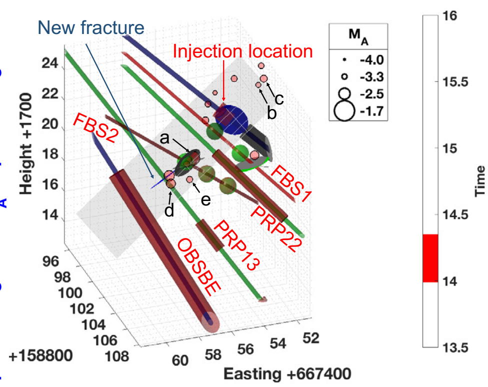

- The FBG sensor in FBS2 at 3.7 m indicates a change in behavior (flattening) at the time the seismic event a) occurs. Shortly afterwards, the interval PRP13 starts to react and at the same time the beforementioned FBG sensor show a slight decrease in tension and stabilizes again.
- The new fracture was observed at a borehole depth of 20 m by the distributed strain system using optical fibers.
- Event b) and c) occur on the other site of the propagating fracture compared to the events a), d) and e)
- Highest increase in pressure is observed during shut-in phase without any located seismic event.
- The located seismic events during the two episodic fracturing cycles indicate an **asymmetric episodic fracturing.**

2. Stick-split mechanism

1. Fluid filled tip building up pressure and increase aperture
2. Tensile failure occurs and pressure drops
3. Fracture closing due to pressure drop brings fluid to the tip
4. Fluid pressure builds up and aperture increase with fluid at the tip

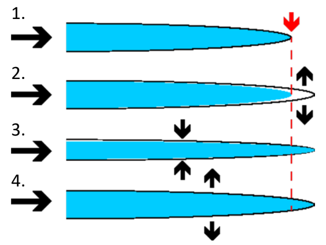

van der Baan et al., 2016

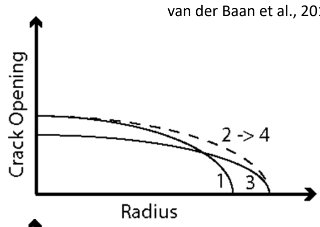

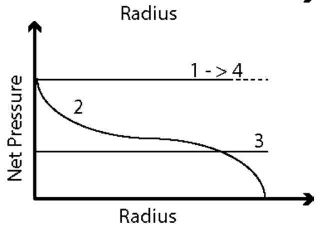

3. Fluid driven fracture solution

The problem can be stated with the following governing equations:

- Elasticity equation
- Lubrication approximation of the non-linear Reynold's equation
- Boundary conditions on both moving fronts:
  - Crack front: $w(\mathbf{x}_c,t)=0, K_I(\mathbf{x}_c,t)=K_{Ic}, \mathbf{x}_c \in C_c(t)$
  - Fluid front: $p_f(\mathbf{x}_f,t)=0, \mathbf{V}_f(\mathbf{x}_f)=\frac{q(\mathbf{x}_f)}{w(\mathbf{x}_f)}, \mathbf{x}_f \in C_f(t)$

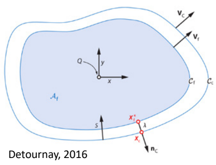

Detournay, 2016

- A **scaling analysis** revealed that the propagation of a penny-shaped fracture in an impermeable medium is characterised by two time-scales and can be presented by a parametric space OMK with three vertices representing a small-time (O), intermediate-time (M) and large-time (K) self-similar solution (Bunger & Detournay, 2007).

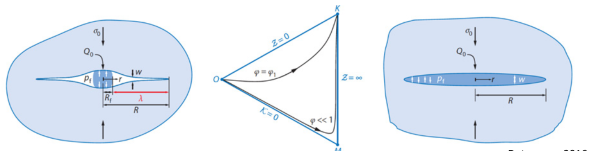

Detournay, 2016

- The **energy dissipation mechanism** corresponds either to the viscous fluid flow (M-vertex) or to the creation of new surfaces (K-vertex). The new length scale for the fluid lag is:

$$\ell_{mk} = \frac{K'^6}{E'^4 \mu'^2 V^2} \approx 1.3 \text{ with } E' = \frac{E}{1-\nu^2},\ K' = \left(\frac{32}{\pi}\right)^{1/2} K_{Ic},\ \mu' = 12\mu$$

using $E = 30\ GPa, \nu = 0.25, K_{Ic} = 0.8\ MPa\sqrt{m}$ and $\mu = 1.2 * 10^{-3}\ Pa * s$, $V = 1 m/s$

Assuming the fracture radius is $R = 4\,m$. This leads to a ratio $\frac{\ell_{mk}}{R} \approx 0.3$ which corresponds to a viscosity-dominated case.

If $K_I(\mathbf{x}_c,t) < K_{Ic}$ during episodic fracturing, the outer boundary does not move until the $K_I(\mathbf{x}_c,t) = K_{Ic}$ is fulfilled. This has a direct influence on the propagation velocity, which decreases when it is averaged over time. We can conclude that the best approximation for the episodic fracturing is a viscosity-dominated case.

Further considerations:

- An asymmetric fracturing behavior, where $K_I(\mathbf{x}_c,t) = K_{Ic}$ changes at the fracture boundary needs to be numerically modelled.
- Asymmetric fracturing is often observed, but what is the driving mechanism behind this effect?

References

- Bunger, A. P., & Detournay, E. (2007). Early-time solution for a radial hydraulic fracture. *Journal of Engineering Mechanics-Asce*, *133*(5), 534–540. https://doi.org/Doi 10.1061/(Asce)0733-9399(2007)133:5(534)
- Detournay, E. (2016). Mechanics of Hydraulic Fractures. *Annual Review of Fluid Mechanics*, *48*(1), 311–339. https://doi.org/10.1146/annurev-fluid-010814-014736
- Van der Baan, M., Eaton, D. W., & Preisig, G. (2016). Stick-split mechanism for anthropogenic fluid-induced tensile rock failure. *Geology*, *44*(7), 503–506. https://doi.org/10.1130/G37826.1

*nathan.dutler@unine.ch

SCCER SoE
SWISS COMPETENCE CENTER for ENERGY RESEARCH
SUPPLY of ELECTRICITY

SCCER-SoE Annual Conference 2018

ÉCOLE POLYTECHNIQUE FÉDÉRALE DE LAUSANNE
Massachusetts Institute of Technology

Supported by:
Schweizerische Eidgenossenschaft
Confédération suisse
Confederazione Svizzera
Confederaziun svizra
Swiss Confederation
Innosuisse – Swiss Innovation Agency

Investigation on Hydraulic Fracturing of Granite

A.de Saussure, L. Laloui[1], H. H. Einstein[2]
[1] Laboratory of Soil Mechanics LMS, Swiss Federal Institute of Technology of Lausanne EPFL, Switzerland
[2] Earth Resources Laboratory ERL, Massachussets Institute of Technology MIT, Cambridge, MA, USA

Motivation and Goals

Enhanced Geothermal Systems (EGS) constitute a large renewable source for electricity production. Hydraulic fracturing permits to increase the permeability of the rock in a naturally fractured environment.

→ Hydraulic stimulation in deep rock to reactivate existing fractures by injecting pressurized water
→ Understand better the mechanisms of hydraulic fracturing for EGS: induce shear failure in Barre Granite

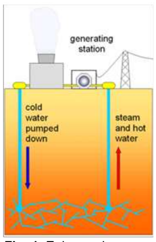

Fig. 1: Enhanced Geothermal System http://climatereach.blogspot.com/.

Methods

The interaction between hydraulic fractures and pre-existing, non-pressurized flaws is investigated experimentally.
The experiments are performed on prismatic specimens of Barre Granite containing two pre-cut flaws under uniaxial or biaxial external load. Fluid is injected in the flaw until failure. Pressure and injected fluid volume are recorded. The crack development is captured with *a high-speed camera* and a high-resolution camera. Shearing is identified under different flaw geometries and loading conditions.

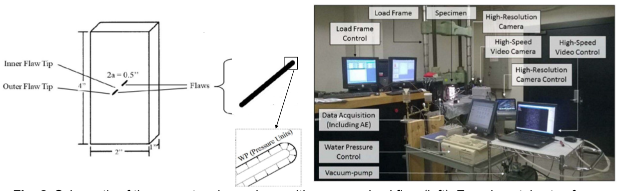

Fig. 2: Schematic of the pre-cut rock specimen with a pressurized flaw (left). Experimental setup for hydraulic fracturing experiments (right).

Analytical investigation on hydrofracturing and hydroshearing

The type of failure (i.e. shear or tensile) is defined by the location of the intersection of the critical Mohr circle with the failure envelope.
The evolution of the stress state around a pressurized opening is observed while the external stress and the internal pressure increase. The tangential stress is determined by an analytical solution (Pollard and Fletcher, 2005) and the normal stress corresponds to the internal fluid pressure. The Mohr circles represent the stress state at various locations around the tip of the opening.

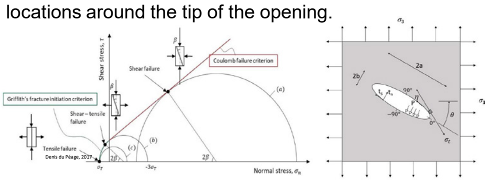

Fig. 3: Failure envelope and Mohr circles corresponding to tensile and shear failure (left), Elliptical flaw in an elastic plate with biaxial stress (right).

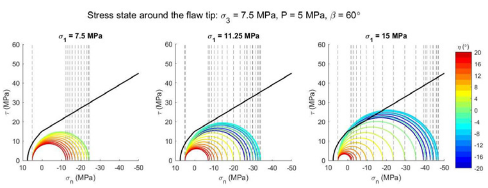

Fig. 4: Effect of an increase of vertical stress on the stress state around the tip of a pressurized flaw leading to shear failure.

Contact: arabelle.desaussure@gmail.com

Types of cracks and grain structure

Different crack types are observed: tensile inter-granular, tensile intra-granular and shear inter-granular cracks. In addition, micro-cracks are observed in the hydroshearing experiments. They are punctual and aligned, linked to the development of a crack, or extended and delimited by grain boundaries.

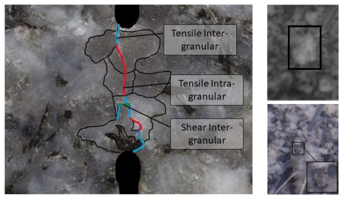

Fig. 5: Type of cracks and grain boundaries (left). White patching: extended zone (top right) and punctual (bottom right) in hydroshearing experiments.

From hydrofracturing to hydroshearing

Tensile failure is observed in the uniaxial experiments whereas shear failure is observed within the biaxial experiments: dilatancy, en echelon crack patterns and sliding. Hydroshearing occurs with a different test procedure corresponding to an increase of vertical stress and a constant internal pressure leading to the intersection of the Mohr circles with the linear part of the failure envelope (Fig. 4).

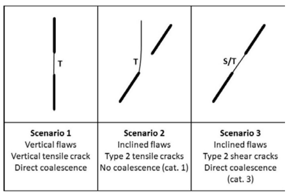

Fig. 6: Crack scenarios with crack types and coalescence categories observed in the uniaxial experiments. Biaxial experiments only show scenario 3.

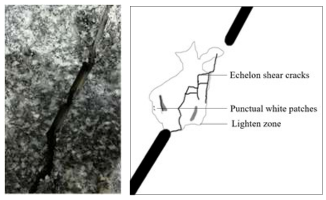

Fig. 7: Frame (left) and sketch (right) of the crack pattern experiencing scenario 3 in a biaxial experiment showing hydroshearing .En echelon cracks, white patching and dilatancy.

Conclusion

The experiments have shown that:
→ Visible cracks propagation and crack patterns are highly influenced by the large grains in Barre Granite
→ Micro-cracks develop in the form of white areas in the shear fracture process zone
→ Hydroshearing is observed under a combination of biaxial external stress and hydraulic pressure.

The identification of the conditions leading to either hydrofracturing or hydroshearing will allow to understand better the difference between both mechanisms and its effect on induced seismicity through acoustic emissions measurements

References

[1] Morgan, S. P., Johnson, C. A., & Einstein, H. H. (2013). Cracking processes in Barre granite: fracture process zones and crack coalescence. *International journal of fracture*, *180*(2), 177-204.

[2] da Silva, B. G., & Einstein, H. (2018). Physical processes involved in the laboratory hydraulic fracturing of granite: Visual observations and interpretation. *Engineering Fracture Mechanics*, *191*, 125-142.

[3] Pollard, D. D. & Fletcher R. C. (2005). *Fundamental of structural geology*. Cambridge University Press.

Advances in laboratory investigation of fluid-driven fractures

Thomas Blum and Brice Lecampion
Geo-Energy Laboratory, EPFL

GeoEnergyLab

1. Introduction

Wide range of applications:

- oil and gas extraction
- geothermal energy recovery
- CO2 sequestration

Need for models to:

- efficiently fracture the targeted formation
- better understand the physics of fluid-driven fracturing
- get an estimate of fracture size and shape during growth

Scaled laboratory experiments:

- allow to validate theoretical predictions
- provide datasets under controlled conditions
- include physical limitations

2. Laboratory setup

- cubic geologic specimen, 250 x 250 x 250 mm
- reaction frame: confining stresses of up to 25 MPa along each axis
- independently controlled pairs of flat-jacks to apply confining stresses
- high-pressure injection pump: flow rate from 1 μL to 90 mL/s
- notch at the bottom of the wellbore for localized initiation
- experiment duration on the order of minutes to a few hours

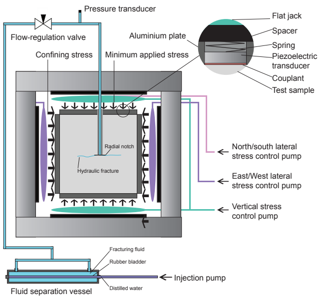

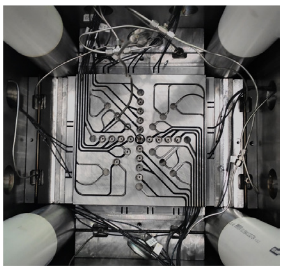

Left: schematic of the experimental setup, Right: top-view photo inside the reaction frame, with flat-jacks and platen on the sides of the specimen, and platen with piezo transducers on the top.

3. Acoustic monitoring

- 64 piezoelectric transducer arranged in 32 sources and 32 receivers
- mix of compression and shear in order to use both P- and S-waves
- sequential excitation of all 32 sources every few seconds for snapshots of the acoustic properties during the fracture propagation

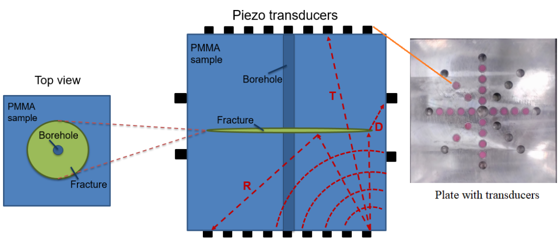

Schematic of the transducer layout and different arrival modes.

- **R** - reflected signal: fluid content of the fracture
- **T** - transmitted signal: fracture thickness
- **D** - diffracted signal: position of the fracture tip.

Transmission coefficient through a planar fluid layer of thickness **h**:

$$T(\omega,h) = \frac{(1-r_{ff}^2)\exp(i\alpha)}{(1-r_{ff}^2)\exp(2i\alpha)} \tag{1}$$

where ω the signal frequency; $r_{ff} = \frac{z_r+1}{z_r-1}$, $z_r = \frac{\rho_f c_f}{\rho_s c_s}$; ρ_s, ρ_f are the densities of the solid and fracturing fluid, respectively; and c_s, c_f the P-wave velocities of the solid and fracturing fluid, respectively.

4. Work progress

- Investigations of Carmen slate: highly bedded anisotropic material, relevant for fracture propagation normal to the bedding plane. Currently issues with notching and fracture initiation.
- Fractures in Carrara marble: propagation in fine-grained material, comparison between toughness- and viscosity-dominated regimes of propagation.

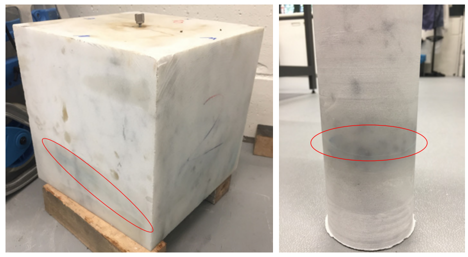

5. Injection in Carrara marble

- No vertical confining stress
- 2 MPa horizontal stresses
- Injection fluid: glycerol, $\eta = 0.6$ Pa.s, flow = 0.02 mL/min

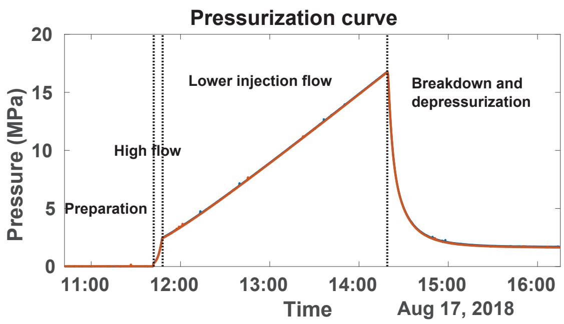

Analysis of transmission measured with one pair of transducers, placed opposite from one another:

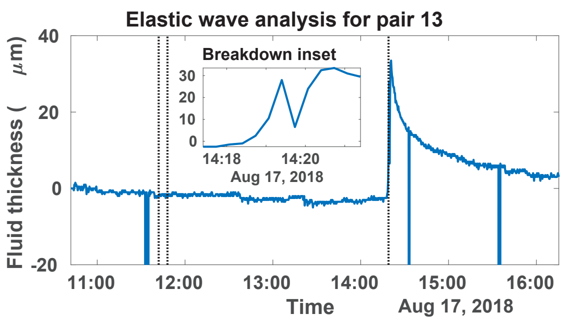

6. Conclusions

Extensive analysis of elastic wave data to follow soon for a diverse set of geologic specimens and experimental conditions.

SCCER-SoE Annual Conference 2018

SCCER SoE
SWISS COMPETENCE CENTER for ENERGY RESEARCH
SUPPLY of ELECTRICITY

Supported by:
Schweizerische Eidgenossenschaft
Confédération suisse
Confederazione Svizzera
Confederaziun svizra
Swiss Confederation
Innosuisse – Swiss Innovation Agency

Building a geological model for analysis and numerical modelling of hydraulic stimulation experiments

H. Krietsch[1], J. Doetsch[1], V. Gischig[2], M.R. Jalali[3], N. Dutler[4], F. Amann[3] and S. Loew[1]
[1]ETH Zurich [2]CSD Ingenieure AG Bern [3]RWTH Aachen [4]University of Neuchâtel

Motivation

We build a geological model (Krietsch et al., 2018a) for the in-situ stimulation and circulation experiment (Amann et al., 2018).
The model is used for:

- High resolution of geological visualization
- As a baseline for a DFN
- Hydraulic characterization
- Geophysical characterization
- Analysis and interpretation of experimental data
- Numerical modelling of the experiment

Geological mapping

The test volume is bound by two tunnels and intersected by 15 boreholes. The mapping included mapping of the tunnels using geodetic measurements and panorama images, pictures of the wet and dry cores, and acoustic and optical televiewer borehole logging. Fig. 1 shows a summary of the mapping approach including the interpolation between tunnels and boreholes.

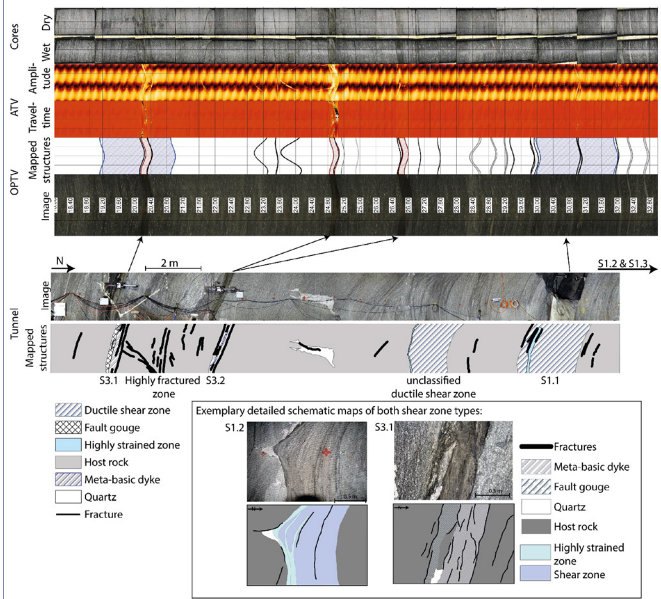

Fig. 1: Summary of geological data, based on which the major shear zones were interpolated. The internal structure of these shear zones (S1 and S3) were mapped in detail. Figure was modified after Krietsch et al., 2018b.

Geological structures

A total of 5 shear zones (3 ductile and 2 brittle-ductile) were mapped. Various brittle fractures (partly open or biotite covered), a pervasive foliation, quartz bands and minor meta-basic dykes were mapped, too (Fig. 2).

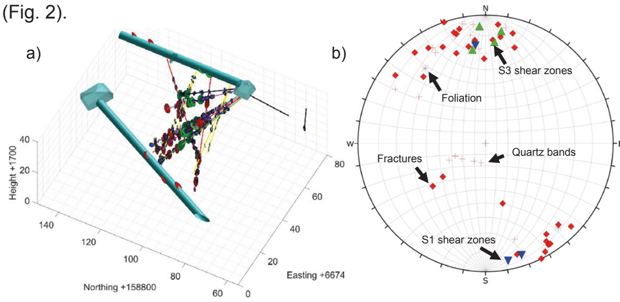

Fig. 2: a) Mapped geological structures inside the test volume, b) orientations of geological structures in a lower hemisphere stereoplot.

Shear zone interpolation steps

- Mapping all shear zones along tunnels and boreholes
- Definition of shear zone sets
- Triangulation between coordinates of each set, neglecting local orientations.
- Third order polynomial interpolation including third order orientations (Fig. 3).

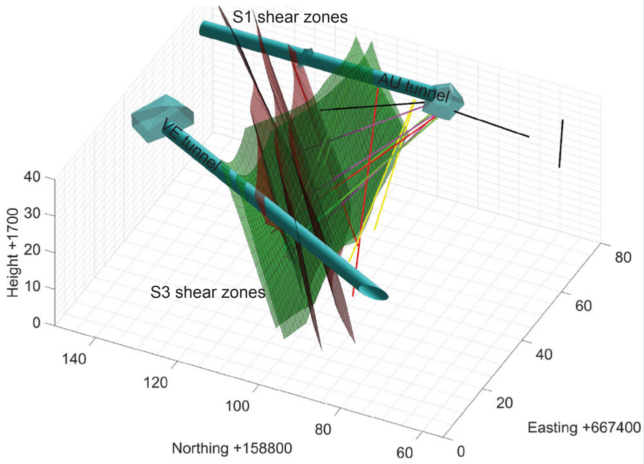

Fig. 3: Interpolated shear zones based on third order polynomial functions.

Technical validation using geophysical methods

Seismic tomography between two tunnels revealed a low velocity zone between two S3 shear zones that correlates with a mapped highly fractured zone (Fig. 4).

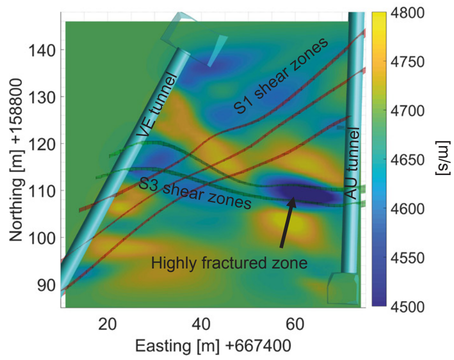

Fig. 4: Seismic tomography with interpolated shear zones.

Summary/Outlook

The geological model represents a high resolution geological baseline visualization of the test volume. It can be used for the construction of a DFN/HydroDFN using e.g., Golder's FracMan, and can be used for setting up a grid for numerical modelling of the stimulation experiment.

References:

Amann et al., 2018 – The seismo-hydro-mechanical behavior during deep geothermal reservoir stimulations: open questions tackled in a decameter-scale in-situ stimulation experiment *Solid Earth, 9, 115-137*
Krietsch et al., 2018a - Comprehensive geological dataset for a fractured crystalline rock volume at the Grimsel Test Site *ETH research collection*
Krietsch et al., 2018b – Comprehensive geological data of a fractured crystalline rock mass analog for hydraulic stimulation experiments *Nature Scientific Data – in review*